

Optimization of a Moving Sensor Trajectory for Observing a Point Scalar Source in Turbulent Flow

C. F. Panagiotou^{1,2†}, D. Cerizza¹, T. A. Zaki³, and Y. Hasegawa¹

¹Institute of Industrial Science, The University of Tokyo, Tokyo, Japan

²Eratosthenes Centre of Excellence, Cyprus University of Technology, Limassol 3036, Cyprus

³Department of Mechanical Engineering, Johns Hopkins University, Baltimore, MD, USA

(Received xx; revised xx; accepted xx)

We propose a strategy for optimizing a sensor trajectory in order to estimate the time dependence of a localized scalar source in turbulent channel flow. The approach leverages the view of the adjoint scalar field as the sensitivity of measurement to a possible source. A cost functional is constructed so that the optimal sensor trajectory maintains a high sensitivity and low temporal variation in the measured signal, for a given source location. This naturally leads to the adjoint-of-adjoint equation based on which the sensor trajectory is iteratively optimized. It is shown that the estimation performance based on the measurement obtained by a sensor moving along the optimal trajectory is drastically improved from that achieved with a stationary sensor. It is also shown that the ratio of the fluctuation and the mean of the sensitivity for a given sensor trajectory can be used as a diagnostic tool to evaluate the resultant performance. Based on this finding, we propose a new cost functional which only includes the ratio without any adjustable parameters, and demonstrate its effectiveness in predicting the time dependence of scalar release from the source.

1. INTRODUCTION

It is well known that animals and insects heavily rely on their advanced olfactory sense for a variety of activities, such as food scavenging, mating and avoiding predators. As a result, humans use the superior sensitivity of animals in various applications. For example, dogs have been extensively used for drug identification, rescue operations and pursuing criminals. Concurrently, the rapid progresses in robotics and sensory systems suggest that mobile robots or vehicles could successfully replace animals. Such technologies should be particularly important for operations under hazardous environments which are inaccessible to humans or animals. In order to achieve those goals, the development of efficient algorithms for characterizing a scalar source based on limited sensor signals in a turbulent environment is important (Kowadlo & Russell 2008; Ishida *et al.* 2012).

Existing algorithms for scalar source identification can be classified into two categories: reactive and model-based algorithms. The former prescribes sensor movement based on a sensor signal. In such a strategy, the flow environment is treated as a black box, and the algorithms for sensor movement are often inspired by the motions of biological organisms (Kennedy & Marsh 1974; Muller & Wehner 1994; Harvey *et al.* 2008). In contrast, the latter explicitly takes into account the mathematical models of fluid flow and associated scalar transport. Although the computational cost for the latter tends to become higher, a

† Email address for correspondence: co.panayiotou@cut.ac.cy

model-based method is expected to show superior performance than a reactive one, since complex dynamics of scalar transport are incorporated in their algorithms. However, their superiority has not been fully verified yet (Voges *et al.* 2014).

The model-based approaches generally result in an optimization problem, in which minimization of a cost functional is required under some constraints. Optimization techniques can generally be categorized into probabilistic (Patan & Patan 2005; Pudykiewicz 1998; Sohn *et al.* 2002; Ucinski 2000) and deterministic methods (Bewley *et al.* 2001; Ucinski & Baranowski 2013). Probabilistic approaches explore a parameter space in a probabilistic way until they reach the global optimum. For example, the infotaxis strategy developed by Vergassola *et al.* (2007) is based on the Bayesian inference and seeks to minimize the Shannon entropy in order to locate the scalar source. Keats *et al.* (2007) proposed a computationally efficient algorithm by combining the adjoint advection-diffusion equation with Monte Carlo Markov Chain sampling to evaluate the posterior probability. Although probabilistic approaches are effective in relatively simple flow configurations, it is not feasible to extend them to unsteady and three-dimensional flow environments, where the degrees of freedom of the design parameters drastically increase.

In the deterministic methods, the set of design parameters are simultaneously optimized based on the associated gradients of a prescribed cost functional. Their unique feature is that the computational cost does not depend on the number of design parameters, although a resultant solution may reach a local optimum. Cerizza *et al.* (2016) developed a deterministic method for estimating the time history of the scalar source intensity at a known source location in a fully developed turbulent channel flow reproduced by direct numerical simulation (DNS). A finite number of stationary sensors were placed in the downstream of the scalar source, and the temporal change of the scalar source intensity was estimated from the downstream sensor signals by applying the adjoint analysis. Using a similar approach, Wang *et al.* (2019) reconstructed the spatial location of the source from remote measurements. In both studies, a scalar source distribution is estimated by solving the adjoint scalar field, which can be interpreted as the sensitivity of a sensor (Keats *et al.* 2007).

The adjoint advection-diffusion equation has a source term at the sensor location, and it is solved backward in time with a negative advection velocity. Consequently, the resultant adjoint scalar field propagates upstream towards possible sources in the past. It can be shown that iterative update of an estimated scalar source based on the adjoint scalar field guarantees a monotonic decrease in the squared error between the true and estimated scalar concentration at a sensor location (Cerizza *et al.* 2016). Cerizza *et al.* systematically changed the streamwise distance between a scalar source and a sensor, and reported the impact on the estimation performance at different pulsation frequencies of the source. They also showed that the estimation performance is drastically improved with increasing the number of sensors. This suggests that the adjoint scalar fields generated at different sensor locations have complementary effects, so that the overall sensor sensitivity at the source location is enhanced.

Although Cerizza *et al.* assumed sensors are stationary, it is expected that higher estimation performance could also be achieved by moving a single sensor along a proper trajectory without increasing a number of sensors. Indeed, there exist several studies which apply deterministic approaches to optimization of sensor arrangement and trajectory. For example, Daescu (2008) conducted numerical experiments on shallow water flows in order to optimize the measurement locations of stationary platforms in the context of the 4D-Var data assimilation, while Misaka & Obayashi (2014) proposed a similar framework in order to effectively reduce the error against unsteady vortical flows. King *et al.* (2014) developed tools for optimal sensor placement for numerical

weather prediction. Particularly, they solved an optimisation problem to select sensor configurations that maximize the observability, a metric which measures the ability to infer the internal state of a system from knowledge of its external outputs, in order to provide a good forecast of weather conditions. Additional works exist (Ucinski & Chen 2006; Tricaud & Chen 2010) that presented a method to obtain the optimal trajectories of a team of robots for the estimation of the system's parameters. However, those authors pointed out that the methods suffer from high computational complexity. As a result, they considered only simplified configurations, particularly diffusive distributed systems without convection, and the complex non-linear sensor dynamics were described by simple ordinary differential equations.

The main objective in the present study is to develop a framework to optimize the trajectory of a moving sensor for scalar source estimation in unsteady three-dimensional turbulent flows. For this purpose, we revisit the physical meaning of the adjoint scalar field as the sensitivity of measurement, and formulate the problem as optimization of the sensitivity of a moving sensor for a given source location. This naturally leads to an extra-adjoint equation, or the adjoint-of the adjoint, based on which the sensor trajectory can be optimized. The obtained sensor trajectory results in an estimation performance as high as those obtained by seventeen stationary sensors.

The current paper proceeds as follows: After describing the flow configurations and the numerical scheme in § 2, we briefly introduce the estimation results of stationary sensors in § 3. In § 4, we develop an optimization strategy for a moving sensor trajectory. Then, the estimation performances of a moving sensor are presented and compared with those by single and multiple stationary sensors in § 5. Summary and conclusions of the present study are given in § 6.

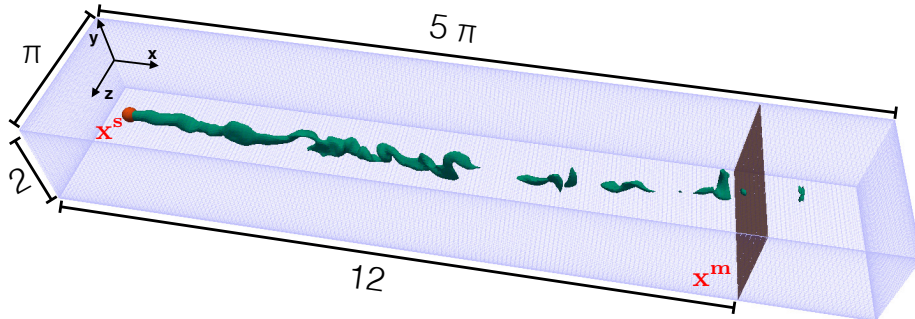


Figure 1: Schematic of the computational domain.

2. COMPUTATIONAL SETUP

We consider a fully developed turbulent channel flow, in which a passive scalar is released from a stationary point source. Throughout the manuscript, all variables are non-dimensionalized by the friction velocity u_τ and the half height of the channel h , unless otherwise stated. Figure 1 shows the computational domain and the coordinate system, where the streamwise, wall-normal and spanwise coordinates are denoted by x , y , z respectively. The dimensions of the computational domain along the streamwise and spanwise directions are set to be 5π and π , respectively. The origin of the coordinate system is located at the channel center, so that $y = -1$ and 1 correspond to the locations of the bottom and top walls, respectively. Throughout this study, the position of the scalar source, denoted as x_i^s , is located at the centerline of the channel, so that $(x^s, y^s, z^s) = (1.1, 0, \pi/2)$. We assume the scalar source location is given, while the time trace of the scalar source intensity is unknown. Hence, our goal is to estimate the scalar source intensity based on the sensor measurement downstream.

The position of a moving sensor is denoted by $x_i^m(t)$ which is in general an arbitrary function of time t . In the present study, the sensor is assumed to move freely in the y - z plane, while its x -coordinate is fixed to $x_1^m = 13.1$. This way, the estimation performances obtained from stationary and moving sensors will be compared under the same streamwise separation of $L_x = 12$ between the source and the sensors. Hereafter, the x -plane where the sensor is located is referred to as a sensing plane.

We assume an incompressible and newtonian fluid, so that its governing equations are given by the following momentum and continuity equations:

$$\frac{\partial u_i}{\partial t} + u_j \frac{\partial u_i}{\partial x_j} = -\frac{\partial p}{\partial x_i} + \frac{1}{Re_\tau} \frac{\partial^2 u_i}{\partial x_j^2}, \quad (2.1)$$

$$\frac{\partial u_j}{\partial x_j} = 0, \quad (2.2)$$

where u_i is the velocity component in the i -th direction and p is the thermodynamic pressure. The flow is driven by a constant mean pressure gradient imposed along the streamwise direction x , and the friction Reynolds number is defined as $Re_\tau = \frac{u_\tau h}{\nu} = 150$,

where ν is the kinematic viscosity. This corresponds to the bulk Reynolds number of $Re_b \equiv U_b(2h)/\nu \approx 4600$, where U_b is the bulk mean velocity. No-slip boundary conditions are imposed at the top and bottom walls, while periodic conditions are applied in the x and z directions.

The transport equation of a passive scalar c is given by

$$\frac{\partial c}{\partial t} + u_j \frac{\partial c}{\partial x_j} = \frac{1}{Pe} \frac{\partial^2 c}{\partial x_j^2} + Q(\mathbf{x}, t), \quad (2.3)$$

where $Q(\mathbf{x}, t)$ is a scalar source, which can be considered as an arbitrary function of space and time. The Peclet number is defined as $Pe = \frac{u_\tau h}{\Gamma}$, while Γ is the coefficient of mass diffusivity of a scalar. Following Cerizza et al., the Peclet number is chosen to be equal to Re_τ , so that the Schmidt number $Sc = Pe/Re_\tau = \nu/\Gamma$ is unity.

Assuming the scalar source is spatially localized and its intensity changes in time as $\phi(t)$, the scalar source can be represented by

$$Q(\mathbf{x}, t) = \phi(t)\delta(\mathbf{x} - \mathbf{x}^s), \quad (2.4)$$

where δ is the Dirac's delta function. In the current study, we approximate the delta function with a steep Gaussian function in order to avoid numerical oscillation,

$$\delta(\mathbf{x} - \mathbf{x}^s) \simeq \left(\frac{\beta}{\pi}\right)^{3/2} \exp(-\beta|\mathbf{x} - \mathbf{x}^s|^2), \quad (2.5)$$

where β is chosen so that the scalar source is distributed over several grid points. The temporal part of the source function $\phi(t)$ is set as

$$\phi(t) = \frac{1}{2} \left\{ 1 + \cos(2\pi ft + \pi) \right\}, \quad (2.6)$$

so that it smoothly changes between 0 and 1 at a single frequency f . The initial and boundary conditions for the scalar field are given as

$$c(\mathbf{x}, t = 0) = 0, \forall \mathbf{x} \in \Omega \quad (2.7a)$$

$$\frac{\partial c}{\partial x_j} n_j = 0 \quad \text{at } y = \pm 1, \quad (2.7b)$$

where n_j represents the outward normal vector on the wall boundary and Ω refers to the entire fluid domain. In addition, we remove the scalar in the proximity of the domain boundaries along the streamwise and spanwise directions in order to avoid the scalar entering from the opposite side by virtue of the periodic conditions

Direct numerical simulation is adopted for solving the velocity and scalar equations. For spatial discretization, we use a pseudo-spectral method, where Fourier expansion is adopted in the x and z directions, while Chebyshev polynomials are used in the y direction. The code has been validated and applied to control and estimation problems in previous studies (Hasegawa & Kasagi 2011; Suzuki & Hasegawa 2017). The numbers of modes are set to be $(N_1, N_2, N_3) = (128, 65, 64)$ along the streamwise, wall-normal and spanwise directions, respectively. 3/2 rule is employed in order to remove the aliasing errors, so that the numbers of the physical grid points are 1.5 times larger in all the directions. The present numerical scheme and condition are essentially identical to those in Cerizza *et al.* (2016), where extensive validation has been performed.

3. Scalar source estimation by stationary sensors

In this section, we first summarize the fundamental mathematical properties of the adjoint scalar field, and discuss its physical interpretation from a viewpoint of scalar source estimation. Then, we will show that the adjoint scalar equation can be naturally derived by minimizing the squared error between the true and estimated scalar concentration at a sensor location. Finally, we present the estimation performances of stationary sensors. These results will provide us reference data to compare with those by a moving sensor in § 5.

3.1. Duality relationship

The adjoint scalar field c^* is defined so that it satisfies the following duality relationship:

$$\langle c^*, \mathcal{N}(c) \rangle = \langle \mathcal{N}^*(c^*), c \rangle. \quad (3.1)$$

In equation (3.1), the bracket indicates the spatio-temporal integration, so that

$$\langle \cdot \rangle = \int_0^T \int_{\Omega} \cdot dV dt, \quad (3.2)$$

whereas \mathcal{N} and \mathcal{N}^* are an advection-diffusion operator and its adjoint, which are respectively defined as

$$\mathcal{N} = \frac{\partial}{\partial t} + u_j \frac{\partial}{\partial x_j} - \frac{1}{Pe} \frac{\partial^2}{\partial x_j^2}, \quad (3.3)$$

$$\mathcal{N}^* = -\frac{\partial}{\partial t} - u_j \frac{\partial}{\partial x_j} - \frac{1}{Pe} \frac{\partial^2}{\partial x_j^2}. \quad (3.4)$$

Substituting $\mathcal{N}(c) = Q$ and $\mathcal{N}^*(c^*) = \delta(\mathbf{x} - \mathbf{x}^m)\delta(t - t^m)$ into equation (3.1) yields

$$\langle c^*, Q \rangle = \langle \delta(\mathbf{x} - \mathbf{x}^m)\delta(t - t^m), c \rangle = c(\mathbf{x}^m, t^m) \equiv M(t^m). \quad (3.5)$$

Here, M can be considered as a signal measured at sensor location \mathbf{x}^m and time t^m .

Equation (3.5) indicates that the inner product between the adjoint scalar field c^* and the source distribution Q is equivalent to the sensor signal $M(t)$. A higher value of c^* means higher contribution of Q at a particular location and time to the integral, thereby the sensor signal. This in turn provides physical interpretation of the adjoint field, that is, the sensitivity of the measurement.

In contrast to the forward operator (3.3) for the scalar field c , the adjoint scalar field has to be solved backward in time by using the advection's velocity with an opposite sign as can be seen from equation (3.4). This is reasonable considering that a sensor signal at a certain location \mathbf{x}^m and time t^m should be caused by a scalar source present upstream at an earlier time.

3.2. Algorithm for scalar source estimation

In the adjoint-based estimation of scalar source, an arbitrary scalar source distribution in time and space is first assumed as an initial guess, and then it is iteratively optimized so as to minimize the error between the estimated scalar concentration and the measurement at sensor locations within a certain time horizon T . Hence, we introduce the following cost function J :

$$J = \int_0^T \frac{1}{2} \sum_k \left\{ c(\mathbf{x}_k^m, t) - M_k(t) \right\}^2 dt, \quad (3.6)$$

where $c(\mathbf{x}_k^m, t)$ is the estimated scalar concentration at the k -th sensor location, whereas $M_k(t)$ is the corresponding measurement. In the present study, the measurement noise is neglected, so that $M_k(t)$ is directly provided from the DNS results. The time horizon is set to be $T = 3$, which is normalized by the friction velocity and the channel half height. This is converted to $T^+ = 450$ in wall units. The corresponding convection distance $L_c^+ = U_b^+ \cdot T^+ \approx 6800$ is around three times the streamwise dimension of the computational box.

Minimizing J under the constraint of the scalar advection-diffusion equation is equivalent to minimizing the following Hamiltonian:

$$H = J - \langle c^* \{ \mathcal{N}(c) - \phi(t)\delta(\mathbf{x} - \mathbf{x}^s) \} \rangle, \quad (3.7)$$

where the adjoint scalar field c^* can be regarded as a Lagrangian multiplier. In the present study, we assume a single point source at a known location \mathbf{x}^s . Hence, our problem is to estimate the temporal change of the source intensity $\phi(t)$.

By applying Fréchet differential to H with respect to $\phi(t)$ and integration by parts, we finally reach at the following expression (see Davide et al. Cerizza *et al.* (2016) for the details of the derivation):

$$H' \equiv \frac{\mathcal{D}H}{\mathcal{D}\phi} \delta\phi = \int_0^T c^*(\mathbf{x}^s, t) \phi'(t) dt. \quad (3.8)$$

Here, the adjoint scalar field should satisfy the following equation

$$\begin{aligned} \mathcal{N}^*(c^*) &\equiv \left(\frac{\partial}{\partial t^*} - u_j \frac{\partial}{\partial x_j} - \frac{1}{Pe} \frac{\partial^2}{\partial x_j \partial x_j} \right) c^* \\ &= \sum_k \left\{ c(x_k^m, t) - M_k(t) \right\} \delta(\mathbf{x} - \mathbf{x}_k^m), \end{aligned} \quad (3.9)$$

under the following initial and boundary conditions:

$$c^*(\mathbf{x}, t^* = 0) = 0, \forall x \in \Omega, \quad (3.10a)$$

$$\frac{\partial c^*}{\partial x_j} n_j = 0 \text{ at } y = \pm 1, \quad (3.10b)$$

where the boundary conditions are periodicity in the spanwise z -direction, $c^* = 0$ at the inlet and outlet of the channel. In equation (3.9), $t^* = T - t$, so that t^* proceeds backward in the physical time t .

According to equation (3.8), the reduction of H is guaranteed when the source intensity is updated through the following expression:

$$\phi^{n+1}(t) = \phi^n(t) - \alpha c^*(\mathbf{x}^s, t), \quad (3.11)$$

where α is a constant and its optimal value is derived in Cerizza *et al.* (2016). For a detailed discussion regarding the method the reader should refer to the referenced work. It should be noted that the present algorithm can be applicable to a moving sensor by simply assuming that \mathbf{x}^m changes in time. In this case, the location of the source term in the adjoint equation (3.9) changes in time accordingly. The above algorithm will be used for estimating a scalar source intensity with a moving sensor in § 5.

3.3. Reference source reconstruction from stationary sensors

In this subsection we repeat the method developed by Cerizza *et al.* (2016) for scalar-source reconstruction to get benchmark data, which will be used in § 5 as reference

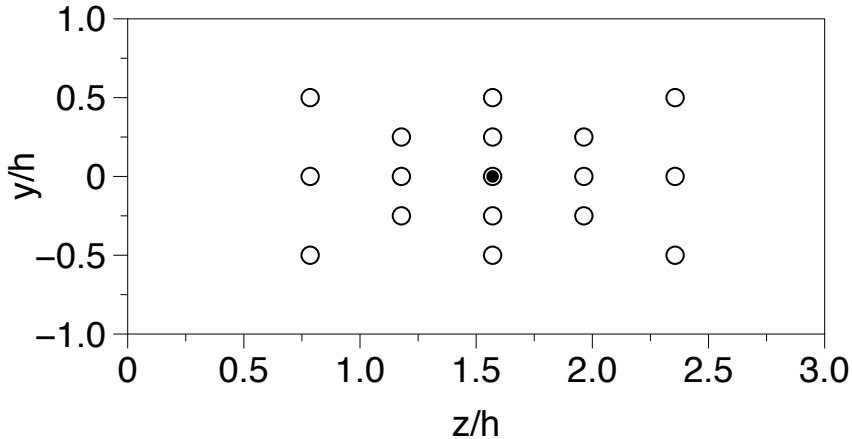


Figure 2: Sensor arrangement in the y - z plane at $x = 13.1$. The open circles correspond to the locations of 17 sensors, whereas the filled circle indicates the location of a single sensor, which is placed at direct downstream of the source.

performance. Following Cerizza *et al.* (2016), we placed stationary sensors downstream the scalar source. Two different sensor placements are considered as shown in figure 2. In the first case, a single sensor is placed directly downstream of the scalar source. In the second case, seventeen sensors are distributed in the crossflow plane, surrounding the central sensor downstream of the scalar source, so that they will cover the mean scalar distribution in the sensing plane.

In figure 3, the time traces of the source intensity estimated from single and seventeen stationary sensors are plotted and compared with the true distribution, when the pulsating frequency of the source is set to be $f = 4$. It is found that employing seventeen sensors yields much better estimation than that of a single sensor. These results suggest that sensor arrangement plays a critical role in estimating a scalar source.

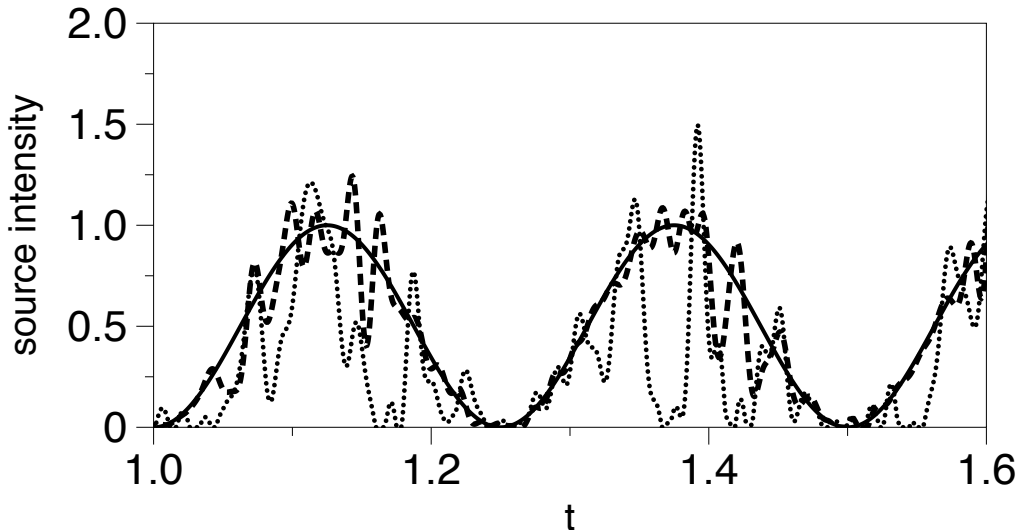


Figure 3: Time trace of source intensity with pulsating frequency $f = 4$. solid line: true profile, dotted line: estimation with a single sensor, dashed line: estimation with seventeen sensors.

4. Strategy for optimizing a sensor trajectory

4.1. Defining cost-functional

The better performance with seventeen stationary sensors shown in the previous section should be attributed to their higher sensitivity at the scalar source location. This suggests that estimation performance could also be improved with a single sensor moving along a proper trajectory, in which possible scalar releases at any instant can be captured by the moving sensor.

Suppose that a point scalar source at a location of \mathbf{x}^s instantaneously releases scalar at an arbitrary time t^s . Such an impulse scalar source may be modeled by $Q(\mathbf{x}, t) = \delta(\mathbf{x} - \mathbf{x}^s)\delta(t - t^s)$. If we assume continuous measurement in time at a sensor location \mathbf{x}^m , the time integral of the sensing signal caused by the impulse release can be obtained by substituting

$$\mathcal{N}^*(c^*) \equiv \frac{\partial c^*}{\partial t^*} - u_j \frac{\partial c^*}{\partial x_j} - \frac{1}{Pe} \frac{\partial^2 c^*}{\partial x_j \partial x_j} = \delta(\mathbf{x} - \mathbf{x}^m), \quad (4.1)$$

into the duality relationship (3.1). This results in

$$\tilde{M}(t) \equiv \int_{-\infty}^{\infty} M(t) dt = \langle c^*, \delta(\mathbf{x} - \mathbf{x}^s)\delta(t - t^s) \rangle = c^*(\mathbf{x}^s, t^s), \quad (4.2)$$

where tilde represents an integral over the time horizon T . When prior knowledge on the scalar release is unavailable, the above equation implies that c^* at the source location should always be kept high with less fluctuation in time in order to detect a possible scalar release within the time horizon.

Based on the above considerations, we define the following cost functional to be minimized in order to find the optimal sensor trajectory:

$$J_1 = -\alpha_1 \int_0^T c^*(\mathbf{x}^s, t) dt + \alpha_2 \int_0^T \left(c^*(\mathbf{x}^s, t) - \bar{c}^*(\mathbf{x}^s) \right)^2 dt + \alpha_3 \int_0^T \mathbf{u}^m \cdot \mathbf{u}^m dt, \quad (4.3)$$

where $\mathbf{u}^m = \frac{d\mathbf{x}^m}{dt}$ denotes the sensor velocity. The positive weighting constants α_1 , α_2 and α_3 are introduced in order to change the relative contribution from each term to J_1 . The first term contributes to increase the averaged sensitivity at the source location, while the second term tends to reduce its temporal fluctuation. The third term represents a penalty on the sensor speed, and works as a regularization term. The time horizon is set to $T = 3$, which is identical to that used for scalar source estimation from a stationary sensor in § 3.

4.2. Parameters for optimizing a sensor trajectory

In order to systematically change the contributions from the three terms in J_1 , we introduce the following two parameters.

The first one is

$$R_{21} = \frac{\alpha_2 \int_0^T \left[c^*(\mathbf{x}^s, t) - \bar{c}^*(\mathbf{x}^s) \right]^2 dt}{\alpha_1 \int_0^T c^*(\mathbf{x}^s, t) dt}, \quad (4.4)$$

which represents the ratio of the second and first terms in J_1 . The weighted constants α_1 and α_2 are determined so as to realize a prescribed value of R_{12} . A large value of R_{21} leads to a larger weight for the second term in J_1 suppressing the temporal fluctuation of c^* at the source location than the first term for maximizing the averaged value of c^* . The second parameter R_{31} corresponds to the ratio of the third and first terms of J_1 , and is defined as

$$R_{31} = \frac{\alpha_3 \int_0^T u_j^m u_j^m dt}{\alpha_1 \int_0^T c^*(\mathbf{x}^s, t) dt}. \quad (4.5)$$

Again, α_1 and α_3 will be adjusted so as to achieve a prescribed value of R_{31} .

Table 1 summarizes all combinations of R_{21} and R_{31} considered in the present study. In Case A, both R_{21} and R_{31} are null, so that only the first term of J_1 is taken into account. On the other hand, for cases B₁-B₄, the weight for the second term is systematically increased while the third term is kept zero. Finally, in case C, the effects of the third term are examined. Note that the time integrals in equations (4.4, 4.5) are in general unknown before optimizing a sensor trajectory. In the present study, their values are evaluated from the statistics of c^* for Case A, so that the values of α_1 , α_2 and α_3 are all fixed during the procedures of optimizing a sensor trajectory.

4.3. Performance indices

Once a sensor trajectory is successfully optimized, it should reduce the temporal fluctuation of c^* with respect to its temporal average \bar{c}^* according to the definition of J_1 in equation (4.3). This motivates us to define the following quantity

$$\epsilon = \frac{\sqrt{\frac{1}{T} \int_0^T \left(c^*(\mathbf{x}^s, t) - \bar{c}^*(\mathbf{x}^s) \right)^2 dt}}{\frac{1}{T} \int_0^T c^*(\mathbf{x}^s, t) dt}, \quad (4.6)$$

which will be used to evaluate different sensor trajectories later.

As for a performance index of scalar source estimation, we define the correlation

Case	R_{21}	R_{31}	circular			random		
			ϵ	ψ^ϕ	ℓ_{norm}^2	ϵ	ψ^ϕ	ℓ_{norm}^2
A	0.0	0.0	1.23	0.74	0.29	1.10	0.80	0.25
B_1	0.1	0.0	1.18	0.76	0.27	1.06	0.82	0.24
B_2	1.0	0.0	0.94	0.77	0.26	0.85	0.89	0.17
B_3	10	0.0	1.30	0.55	0.39	1.17	0.58	0.36
B_4	∞	0.0	1.39	0.53	0.40	1.25	0.55	0.37
C	1.0	1.0	1.03	0.69	0.31	0.97	0.74	0.28
	initial		1.82	0.43	0.46	1.64	0.52	0.42

Table 1: Summary of the numerical conditions and the resultant estimation performance.

coefficient ψ^ϕ between the time traces of the true and estimated source intensities i.e., $\phi^{true}(t)$ and $\phi^{est}(t)$ as

$$\psi^\phi = \frac{\int_0^T (\phi^{true}(t) - \overline{\phi^{true}})(\phi^{est}(t) - \overline{\phi^{est}}) dt}{\sqrt{\int_0^T (\phi^{true}(t) - \overline{\phi^{true}})^2 dt} \sqrt{\int_0^T (\phi^{est}(t) - \overline{\phi^{est}})^2 dt}}. \quad (4.7)$$

Obviously, ψ^ϕ closer to unity indicates a better performance.

Another index is the L2 norm of the difference between $\phi^{true}(t)$ and $\phi^{est}(t)$, given by

$$\ell_{norm}^2 = \sqrt{\frac{1}{T} \int_0^T (\phi^{true}(t) - \phi^{est}(t))^2 dt}. \quad (4.8)$$

A smaller value of ℓ_{norm}^2 means a less estimation error, and thereby better estimation. In the following sections, ψ^ϕ and ℓ_{norm}^2 will be used to evaluate the estimation performances in all cases.

4.4. Derivation of optimization algorithm

Minimizing J_1 given by equation (4.3) requires to optimize the adjoint scalar field which is governed by equation (4.1). Hence, we define the following Hamiltonian for optimizing a sensor trajectory:

$$H = J_1 + \left\langle \theta \left\{ \frac{\partial c^*}{\partial t^*} - u_j \frac{\partial c^*}{\partial x_j} - \frac{1}{Pe} \frac{\partial^2 c^*}{\partial x_j \partial x_j} - \delta(\mathbf{x} - \mathbf{x}^m) \right\} \right\rangle, \quad (4.9)$$

where θ is a Lagrangian multiplier, and can also be considered as the adjoint of the adjoint field. Our purpose is to optimize the sensor trajectory $\mathbf{x}^m(t)$ to minimize H . For this purpose, we can take a standard approach, which is essentially the same as equations (3.7)-(3.11) used for estimating scalar source. Namely, applying the Fréchet differential to equation (4.9) with respect to an infinitesimal change $\delta \mathbf{x}^m$ of a sensor trajectory, and integrating by parts (see Appendix A for more details), we end up with

$$\begin{aligned} \frac{\mathcal{D}H}{\mathcal{D}\mathbf{x}^m} \delta \mathbf{x}^m &\equiv H' = \left\langle -\frac{\partial \theta}{\partial x_j} \delta(x_j - x_j^m) x_j^{m'} \right\rangle - 2\alpha_3 \int \frac{d^2 x_j^m}{dt^2} x_j^{m'} dt \\ &= \int_0^T - \left[\left(\frac{\partial \theta}{\partial x_j} \right)_{\mathbf{x}^m} + 2\alpha_3 \frac{d^2 x_j^m}{dt^2} \right] x_j^{m'} dt, \end{aligned} \quad (4.10)$$

where θ has to satisfy the following equation:

$$\frac{\partial \theta}{\partial t} + u_j \frac{\partial \theta}{\partial x_j} = \frac{1}{Pe} \frac{\partial^2 \theta}{\partial x_j^2} + \left\{ \alpha_1 - 2\alpha_2 (c^* - \bar{c}^*) \right\} \delta(\mathbf{x} - \mathbf{x}^s), \quad (4.11)$$

with the following initial and boundary conditions

$$\theta(\mathbf{x}, t = 0) = 0, \quad \forall \mathbf{x} \in \Omega \quad (4.12)$$

$$\frac{\partial \theta}{\partial x_j} n_j = 0, \quad \text{at } \partial\Omega. \quad (4.13)$$

Equation (4.10) indicates that H' is always negative if the sensor trajectory is updated based on the following expression:

$$x_j^{m'}(t) \left(\equiv x_j^{m,n+1}(t) - x_j^{m,n}(t) \right) = \alpha^n \left[\left(\frac{\partial \theta}{\partial x_j} \right)_{\mathbf{x}^m} + 2\alpha_3 \frac{d^2 x_j^m}{dt^2} \right]^n, \quad (4.14)$$

where the superscript n indicates the current iteration step and α is a positive coefficient determining the amount of the update in each iteration step.

Algorithm 1: Algorithm for optimizing sensor trajectory

- $n = 0$;
 - Solve equations (2.1, 2.2) and store all data regarding the velocity field;
 - Prescribe an initial guess of the sensor trajectory $\mathbf{x}^{m,0}$;
- while** *Convergence criterion is not satisfied* **do**
- Advance the adjoint equation $\mathcal{N}^*(c^*) = \delta(\mathbf{x} - \mathbf{x}^m)$ and record c^* at the source location to evaluate $\bar{c}^* = \frac{1}{T} \int_0^T c^*(\mathbf{x}^s, t) dt$;
 - Advance the adjoint-of-adjoint equation (4.11) for θ and store $\frac{\partial \theta}{\partial x_j}$ at sensor location for the entire time period;
 - Compute step size, $\alpha^n = 0.05 / \max \left| \left[\left(\frac{\partial \theta}{\partial x_j} \right)_{\mathbf{x}^m} + 2\alpha_3 \frac{d^2 x_j^m}{dt^2} \right]^n \right|$;
 - Update sensor's trajectory in accordance with equation (4.14);
 - $n = n + 1$
- end**
-

The overall procedure for optimizing a sensor trajectory is summarized in algorithm 1. First, we solve equations (2.1, 2.2) and store the spatio-temporal evolution of the entire velocity field within the computational domain Ω and the time horizon $0 \leq t \leq T$. This has to be done only once before starting optimization, and the same data set of the velocity field can be used throughout the following optimization procedures. Secondly, assuming an arbitrary initial sensor trajectory $\mathbf{x}^{m,0}$, the adjoint equation (4.1) is solved backward in time and c^* at the source location is recorded. Then, this information is used to solve the extra-adjoint equation (4.11) for θ . Note that, in contrast to equation (4.1), equation (4.11) is solved forward in the original time t . Once θ at the sensor location is obtained, the sensor trajectory is updated in accordance with equation (4.14). The above procedures are repeated until the sensor trajectory converges.

We considered two different initial trajectories which are both lying sufficiently close to the core of the plume at the measurement plane, so that a sensor receives significant signals. The first one is a circular motion, the center of which is located at the channel center and its radius is 0.2, and the second one is a trajectory generated by a random walk starting from the channel center. These two initial trajectories are depicted in figure 4, in which the iso-lines of the mean scalar concentration from the point source at \mathbf{x}^s with

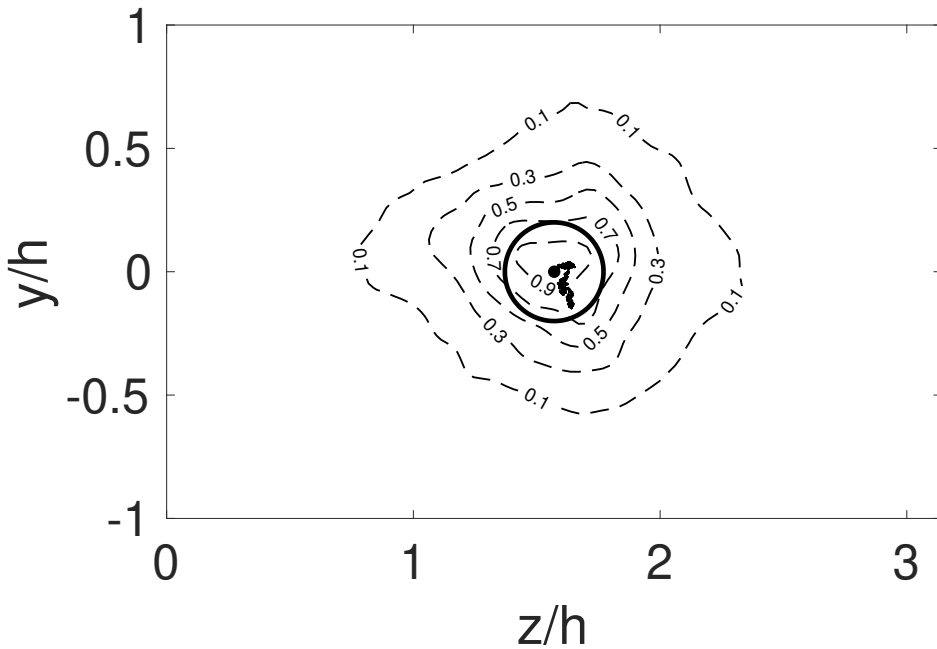


Figure 4: Isolines of the averaged scalar field c at the y - z plane of motion, where the scalar field is time-averaged within the time interval $t \in (0, T)$. The values of the scalar field are normalized to the maximum averaged value. Solid lines indicate the initial sensor trajectories.

a steady release are also shown. It can be confirmed that both initial trajectories are within these contours.

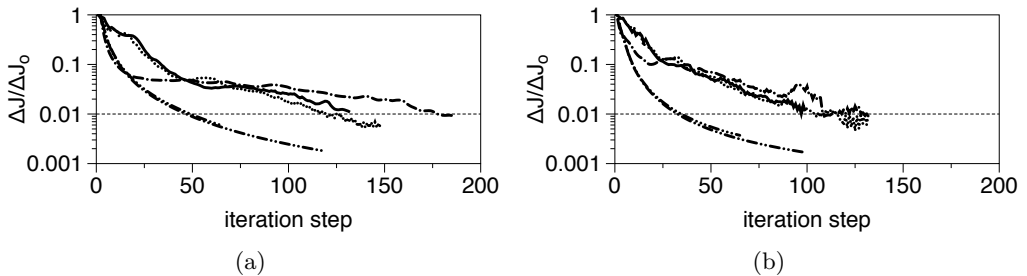


Figure 5: Evolution of cost-functional convergence rate starting from (a) circular and (b) random trajectories. (—) $R_{21} = 0.0$; (·····) $R_{21} = 0.1$; (-·-·) $R_{21} = 1.0$; (- - -) $R_{21} = 10.0$ (- - -) $R_{21} \rightarrow \infty$. A thin horizontal lines corresponds to $\Delta J/\Delta J_0$ which is used to judge the convergence of each optimization.

5. Results

We first show the optimal sensor trajectories obtained for Cases *A-C* in § 5.1. In § 5.2, the estimation performances based on the signals obtained from the optimal sensor trajectories are presented and compared with those of stationary sensors. Based on the obtained results, we propose a simpler and more effective strategy for optimizing a moving sensor trajectory, and validate its performance in § 5.3.

5.1. Optimal sensor trajectory

5.1.1. Cases *A* and *B*

First, we consider cases *A* and *B*, in which the penalty of the sensor velocity is neglected. Figure 5 shows the evolution of the cost functional convergence rate $\frac{\Delta J}{\Delta J_0} = \frac{J_1^n - J_1^{n-1}}{J_1^n - J_1^0}$ as a function of a number of iterations. In the current study, the iteration for optimizing a sensor trajectory is continued until the reduction of the cost functional becomes less than 1% of the initial update, which is depicted by a thin horizontal line.

Figure 6 shows the impact of R_{21} on the evolution of the cost functional (4.3) with the initial sensor trajectory generated by a random walk. Throughout the iterations, the first term in equation (4.3) is dominant for $R_{21} = 0.1$, whereas the second term becomes a primary factor for $R_{21} = 10$. These results indicate that the relative importance of the first and second terms in the cost functional (4.3) can be successfully controlled by changing R_{21} . Note that similar trends are also confirmed when the optimization is initiated from a circular trajectory (not shown here).

Figure 7 shows the time trace of the adjoint field c^* at the source location obtained by the sensor trajectories optimized with different R_{21} from an initially random trajectory. Here, the horizontal axis is $t^* = T - t$, so that it proceeds backward in the original time t . It can be observed that c^* is absent during the initial period of $0 \leq t^* \leq 0.7$. This period corresponds to a time interval for the adjoint field generated at the sensor location reaches at the source location. Indeed, considering the advection velocity at the channel center is $u_c \approx 18$, and the streamwise distance between the sensor and the source is $L_x = 12$, the convection time is approximated as $T_c \approx L_x/u_c = 0.67$, which agrees well with the above initial period.

It is also found that the optimal sensor trajectories with large R_{21} suppress the fluctuation of c^* , whereas those with small values tends to increase the intensity of c^* with larger fluctuations. In order to quantify the fluctuation of c^* relative to its mean, ϵ

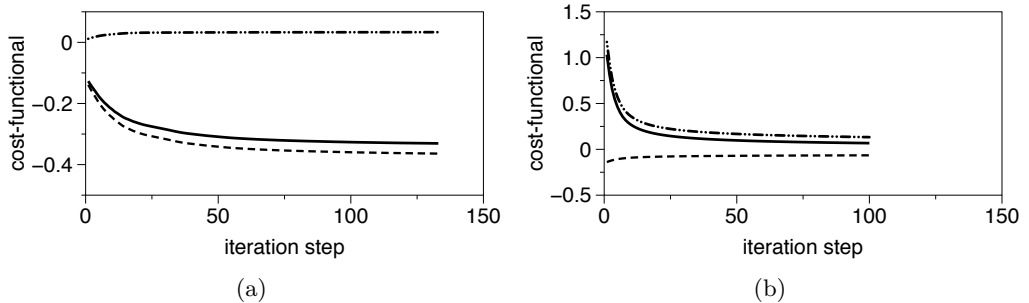


Figure 6: Evolution of the total cost-functional and its individual components for (a) $R_{21} = 0.1$ and (b) $R_{21} = 10$, for an initially random trajectory. (—): the total cost-functional, (----): the first component, (-·-·-): the second component.

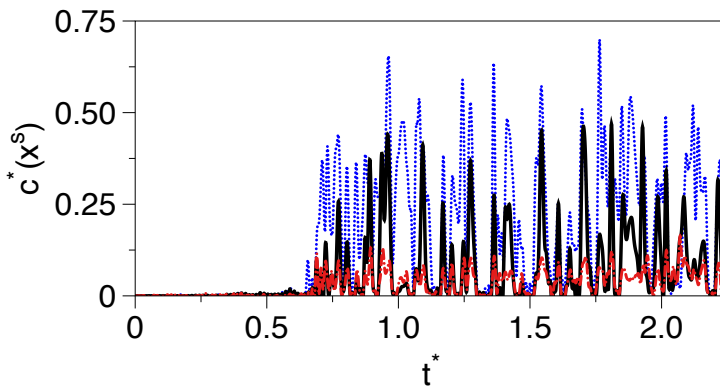


Figure 7: Time trace of the adjoint field at the source location for an initially random trajectory. (—): the initial trajectory, (·····): $R_{21} = 0.1$, (- - -): $R_{21} = 10$.

defined in equation (4.6) is calculated and the results are listed for all cases in Table 1. It is found that ϵ shows a non-monotonic relationship with R_{21} , and reaches its minimum at $R_{21} = 1$ regardless of the initial sensor trajectories. As will be shown later, large sensitivity with less fluctuation in time is a key for better estimation, and ϵ is generally correlated with the resultant estimation performance.

Figure 8 shows the time trace of the y -coordinate of the sensor trajectories optimized from random and circular ones.

It is found that a smaller R_{21} yields more spread sensor trajectory from the center line, i.e., $y = 0$, and quicker changes of sensor location, indicative of high velocities and sudden changes in the sign of sensor's velocity.

Furthermore, the correlation coefficient between the optimal trajectories starting from circular and random trajectories was found to increase with decreasing value of R_{21} . The above observations are related to the source term that appears as the last term on the RHS of equation (4.11). For small R_{21} , this term tends to become constant, thus independent of sensor trajectory. Additionally, the constant source term produces smoother scalar field than a transient source term, making it easier for the sensor to “escape” from local minima and conduct a broad search. A similar trend is also observed

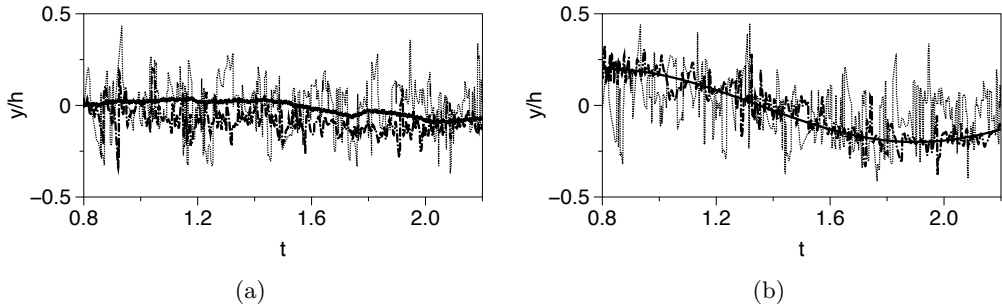


Figure 8: Time trace of the sensor's trajectory along the y coordinate starting from (a) random and (b) circular trajectories. (—): the initial trajectory, (.....): the optimal trajectory with $R_{21} = 0.1$, (— · —): the optimal trajectory with $R_{21} = 10$.

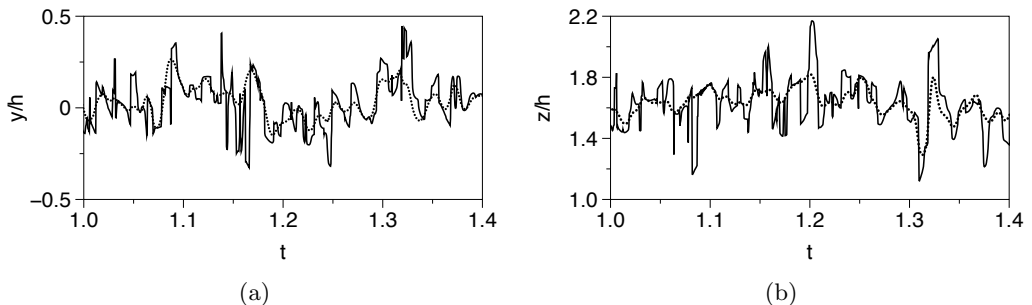


Figure 9: Time traces of the (a) normal and (b) spanwise coordinate of the optimal sensor trajectory starting from a random trajectory. (—): Case B2 (.....): Case C

for z coordinate of the sensor trajectory (not shown here).

5.1.2. Case C

Figure 9 shows the time traces of the sensor trajectories with and without the penalty of the sensor speed (Cases C and $B2$). We observe that non-zero value of R_{31} (Case C) yields a smoother trajectory compared to $R_{31} = 0$ (Case $B2$). This is consistent with the presence of the penalty term (the third term) in the cost functional (4.3).

Figures 10a-b show the time trace of sensor speed along y and z directions respectively for the two cases. To make comparison with the advection scalar velocity, sensor speed is normalized by the bulk fluid velocity \bar{u}_b . Regarding Case C , we observe that the sensor speed is less than the bulk velocity for the majority of the time period, yielding average values $|u_y^m|^+ = 8.5$ and $|u_z^m|^+ = 10.5$. In the absence of velocity restrictions, sensor moves much faster than the bulk velocity in many time instances (average values $|u_y^m|^+ = 26$ and $|u_z^m|^+ = 29$). Consequently, we observe the significant impact that the penalisation term has on sensor speed, thus yielding speeds comparable to the bulk velocity of the mean flow. Comparison between sensor velocity and the fluid movement along the y - z plane is shown in figures 10c-d. Due to the absence of mean flow movement along the plane, the corresponding *rms* values at the centreline are chosen as the characteristic fluid velocities. For both directions, sensor moves at speeds much higher than the *rms* of

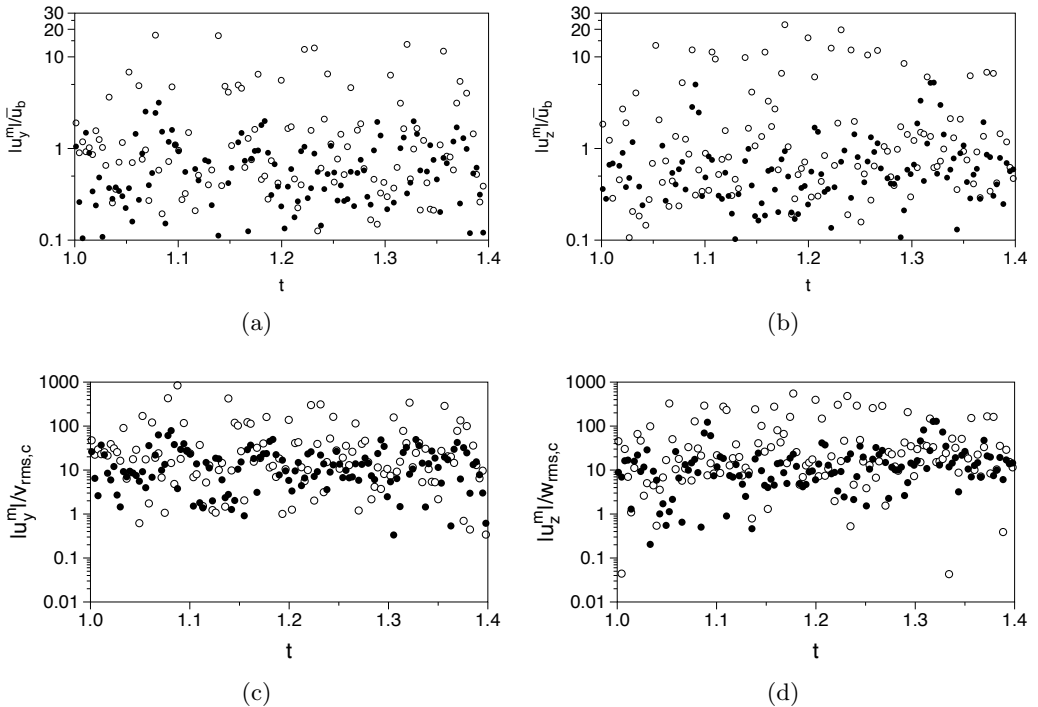


Figure 10: *Top*: Time trace of sensor velocity along (a) wall-normal and (b) spanwise directions, normalized by the bulk fluid velocity. *Bottom*: Time trace of sensor velocity along (c) wall-normal and (d) spanwise directions, normalized by the corresponding *rms* values at the centreline. Filled and open circles denote cases *C* and *B2* respectively.

flow fluctuations. For the majority of the simulation period in case *C*, the sensor speed is more than 10 times higher than *rms* fluctuations (average values around 24 and 27 along *y* and *z* directions). Regarding case *B2*, we observe spikes of the velocity ratio at frequent occurrences, thus leading to much higher velocity ratios (average value around 45 for both components). Thus, we observe that the penalisation on sensor speed results in comparable values between sensor speed and *rms* velocities.

Figure 11 shows the time traces of the adjoint fields at the source location which are generated from the optimal trajectories in Cases *B2* and *C*. It is observed that the fluctuation of the adjoint field becomes larger in Case *C*, where the penalty of the sensor speed is taken into account. This implies that the smoother trajectory is obtained in exchange for the stabilization of the adjoint field. This is also reflected to the increase of ϵ in Case *C* (see, Table 1).

5.2. Scalar source estimation with optimal sensor trajectory

In the previous subsection, it was shown that the parameters R_{21} and R_{31} defined by equations (4.4, 4.5) successfully change the relative importance of the three terms consisting the cost functional (4.3), and the corresponding optimal sensor trajectories are obtained under the compromise of the three terms. Here, we evaluate the performances of scalar source reconstruction based on the signals obtained from the optimal trajectories.

Table 1 summarizes the reconstruction performances evaluated by the correlation coefficient ψ^ϕ and the L2 norm ℓ^2 . It is found that the optimal trajectories generally

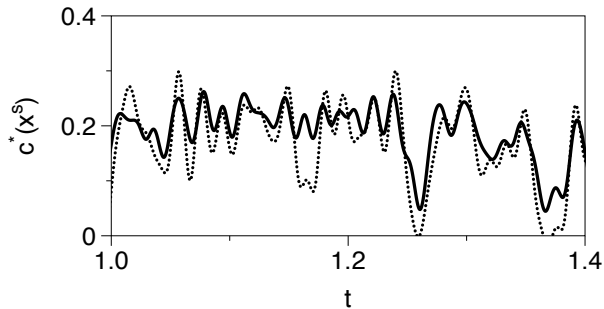


Figure 11: Time trace of the adjoint field at the source location generated from the trajectories optimized from the initially random trajectory. — : Case B2, : Case C

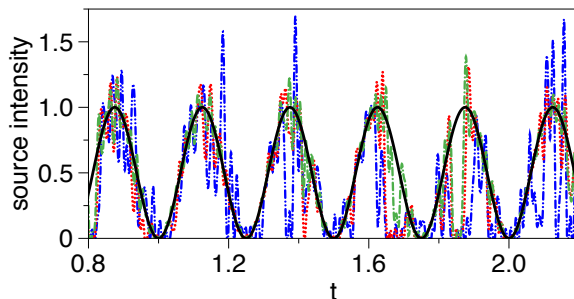


Figure 12: Time trace of the source intensity at the source location for initially random trajectory. Solid line (—) refers to the true profile, dotted line (.....) refers to Case B1, dashed dotted line (-.-.-) refers to Case B2 and dashed double dotted line (-.-.-) refers to Case B3. Only a limited time frame of the entire time horizon considered is shown.

perform much better than the initial circular/random trajectory, and also the single stationary sensor. It should be also noted that the highest performance is commonly obtained in Case *B2* regardless of the initial sensor trajectory.

In figure 12, the true and estimated scalar source intensities are plotted. In consistent with Table 1, the estimation with the optimal trajectory in Case *B2* shows the best match with the true profile.

In order to explain the best estimation performance in Case *B2*, the adjoint scalar field at the source location for the initial random trajectory and the optimal trajectory are compared in the top figure of figure 13, whereas the resultant reconstruction of the scalar source is shown in the bottom. It can be seen that the estimation error is strongly correlated with the fluctuation of the adjoint field at the source location. A larger fluctuation generally causes a large deviation of the estimation from the true profile. Especially, the presence of time periods with no significant adjoint field in the initial trajectory results in the failure of estimation during these periods. These results justify the current setting of the cost functional (4.3) and also suggest that ϵ can be used as a diagnostic parameter for the estimation capability. Indeed, as shown in Table 1, the estimation performance is negatively correlated with ϵ .

Additionally we consider the effects of the penalty of the sensor speed on the estimation

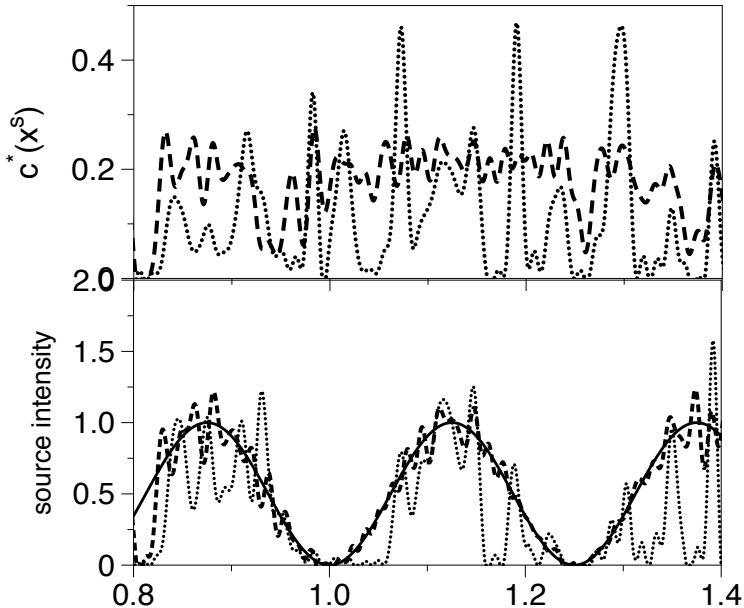


Figure 13: Source profile and adjoint field for a sensor starting from random trajectory. *At top*: Time trace of the adjoint field at the source location. *At bottom*: Time trace of the scalar signal at the source location. Solid line refers to the true profile, dashed line (----) refers to $R_{21} = 1$ and dotted line (.....) refers to the random trajectory.

performance. As shown in figure 11, the adjoint field at the source location in Case *C* shows large fluctuation than that in Case *B2*. As a result, ϵ is increased and the estimation performance is deteriorated (see, Table 1). Adding the penalty term in the cost functional (4.3) results in a smoother trajectory at the cost of larger fluctuation of the adjoint field at the source location. This explains the worse performance in Case *C*.

5.3. Cost functional with ϵ

One of the main issues in the cost functional (4.3) is that it requires to find the optimal values of the weighting coefficients, i.e., R_{21} and R_{31} . Especially, the value of R_{21} is important to determine the relative importance of the first and second terms in equation (4.3). According to the present results, however, the estimation performance is well correlated with a single quantity, i.e., ϵ , throughout all the cases considered. This motivates us to define the following cost functional:

$$J_2 = \frac{c_{rms}^*(\mathbf{x}^s)}{c^*(\mathbf{x}^s)}. \quad (5.1)$$

The advantage of introducing the above cost functional is that there is no adjustable parameter.

Following the same procedure as described in § 4.4, we obtain the following adjoint-of-the-adjoint equation for θ (see Appendix B for the detailed derivation):

$$\frac{\partial \theta}{\partial t} + \frac{\partial(\theta u_j)}{\partial x_j} = \left\{ \frac{\partial}{\partial x_j} \left(\frac{1}{Pe} \frac{\partial \theta}{\partial x_j} \right) \right\} + \frac{1}{T} \left(\frac{c_{rms}^*}{c^{*2}} - \frac{[c^* - \bar{c}^*]}{c^* c_{rms}^*} \right) \delta(\mathbf{x} - \mathbf{x}^s), \quad (5.2)$$

whereas the formula for updating the sensor trajectory is the same as equation (4.14).

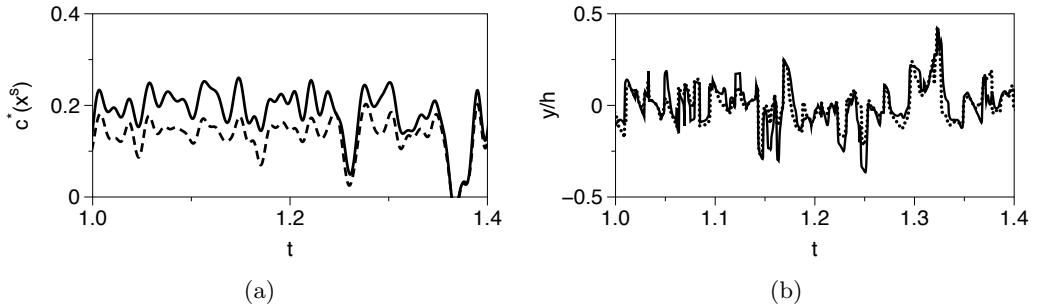


Figure 14: Comparison between the alternative strategy (----) and the optimal case $R_{21} = 1$ of the initial strategy (—), for a sensor initially at rest at the centerline point. (a) Time trace of the adjoint field at the source location for a limited time horizon. (b) Time trace of the normal coordinate of sensor trajectory.

The above equation can be regarded as a modified version of equation (4.11), in which the weighted coefficients α_1 and α_2 are replaced with the statistics of c^* .

As for the initial condition, we consider a stationary sensor located directly downstream of the source. This location was chosen, since it results in the minimum ϵ in the sensing plane when a sensor is stationary.

Figure 14a shows the adjoint fields at the source location for the sensor trajectories optimized by the original cost functional (4.3) with $(R_{21}, R_{31}) = (1.0, 0)$ (Case B_2) and the newly introduced cost functional (5.1). Although the new cost functional yields a slightly lower adjoint field than the original one, the values of ϵ in both cases are similar and around 0.85 after optimization.

The time traces of the wall-normal coordinate of the optimal sensor trajectories are compared in figure 14b. It is confirmed that the sensor trajectories obtained from the original and new cost functionals are similar. The results shown in figure 14 indicate that the new cost functional (5.1) without any adjustable parameter is a potential alternative to the original cost functional (4.3) with the optimal values of R_{21} and R_{31} .

In order to demonstrate the connection between sensor's performance and the new cost functional J_2 , we plot the predictions for the correlation coefficient ψ^ϕ , obtained at every ten iteration steps of the iterative process, as a function of the adjoint ratio c_{rms}^*/\bar{c}^* (figure 15). We observe that the estimation ability of the algorithm increases with decreasing adjoint ratio, in accordance with the present results.

The time traces of the true and reconstructed source intensity at $f = 4$ are shown in figure 16. The figure includes the estimated source intensities based on a single mobile sensor whose trajectory is optimized by the cost functional J_1 in Case B_2 and the new cost functional J_2 . Also, the estimations with a single and seventeen stationary sensors are plotted for comparison. It can be confirmed that the estimation performance of the single mobile sensor is as good as that of seventeen stationary sensors.

The present optimization strategy is based on the idea to maintain the sensor sensitivity at a source location throughout the entire time horizon. Hence, the resultant optimal trajectory should be effective at different pulsating frequencies. Table 2 summarizes the estimation quality obtained from a single movable sensor whose trajectory is optimized by the new cost functional (5.1), and single and multiple stationary sensors at different pulsating frequencies of the source, $f = 2, 4, 8$ and 16. We observe that the estimation performance gradually deteriorates with increasing f in all cases. The single mobile sensor

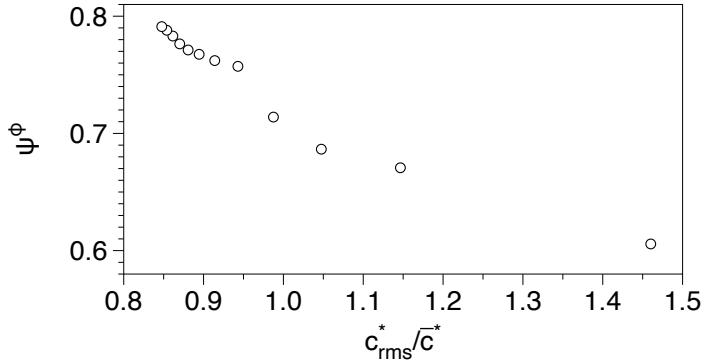


Figure 15: Correlation coefficient ψ^ϕ as a function of adjoint ratio c_{rms}^*/\bar{c}^* for a mobile sensor whose trajectory is optimized with the new cost functional J_2 . Each open circle refers to a different iteration step of the iterative process.

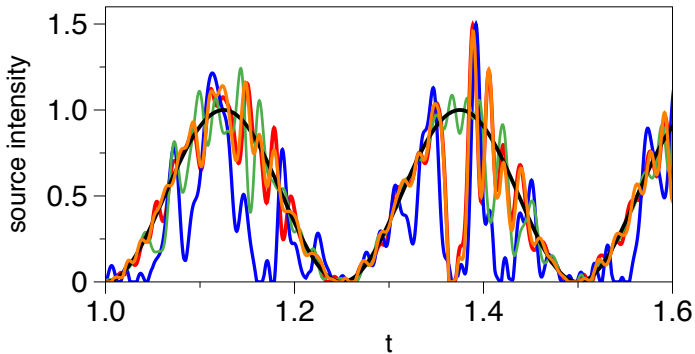


Figure 16: Time evolution of the reconstructed source profiles for $f = 4$. black: true, red: a mobile sensor whose trajectory is optimized with the new cost functional (5.1), orange: a mobile sensor whose trajectory is optimized with the original cost-functional (case *B2*), blue: a single stationary sensor, green: 17 stationary sensors. Only a limited time frame of the entire time horizon is shown.

with the optimal trajectory shows significant improvement compared with the single stationary sensor, and its performance is close to that of seventeen stationary sensors.

5.3.1. Mitigation of dispersion effects

In order to mitigate the effects of dispersion, Cerizza *et al.* (2016) examined how increasing the number of sensors can reduce the loss of signal. Following the same approach, we consider the amount of signal captured by a single moving sensor optimized by the new cost-functional J_2 , and compare it with the signal collected by a single sensor placed at the centerline and seventeen stationary sensors (figure 17a). Compared to the single stationary case, the other two cases mitigate dispersion effects since they are able to capture more mass of the scalar plume. In particular, multiple sensors provide the highest sensor signal (in total), while the moving sensor is able to mitigate dispersion effects by capturing higher fraction of the scalar patches passing through the y - z plane than the single stationary sensor.

f	Stationary		Multiple ($n = 17$)		Movable (J_2)	
	Single	ℓ_{norm}^2	ψ^ϕ	ℓ_{norm}^2	ψ^ϕ	ℓ_{norm}^2
2	0.54	0.40	0.96	0.10	0.83	0.22
4	0.60	0.38	0.94	0.13	0.80	0.24
8	0.49	0.41	0.93	0.13	0.84	0.21
16	0.49	0.40	0.93	0.13	0.86	0.20

Table 2: Summary of the predictions for the statistics at different source frequencies using the new cost-functional J_2 for a single moving sensor. Results for the root-mean square value of the scalar fluctuations are obtained by averaging the sensor signal over the entire time horizon.

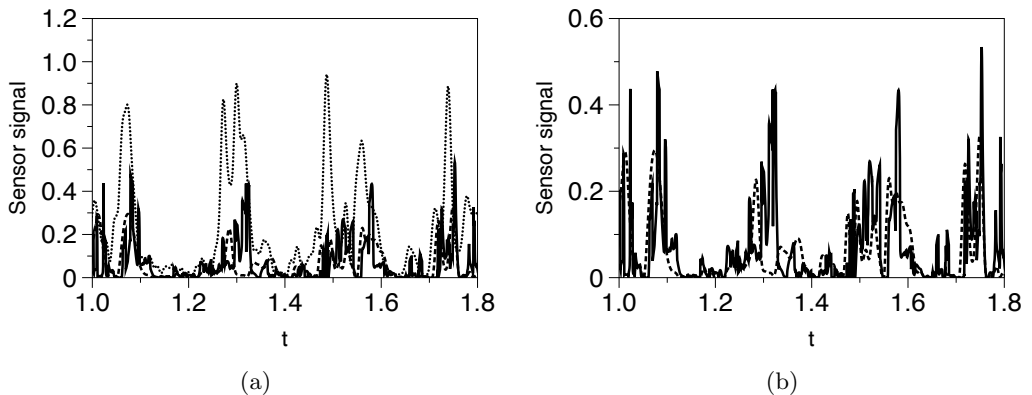


Figure 17: Time trace of the sensor signal with pulsating frequency $f = 4$. Solid line denotes the movable sensor, dashed line (----) denotes the single stationary sensor and dotted line (.....) denotes the seventeen stationary sensors. Only a limited time frame of the entire time horizon is shown.

6. Summary and Conclusions

In the present study, we consider a problem of scalar source estimation in a turbulent environment. Assuming that the location of a point scalar source is known, the time evolution of the source intensity is estimated based on the signals obtained from a sensor located downstream. Particularly, we focus on developing a new strategy for optimizing a trajectory of a moving sensor.

The key idea behind the present optimization strategy is to maximize the sensor sensitivity and minimize its temporal fluctuation at the source location, whereas the sensor sensitivity is theoretically given by the adjoint scalar field generated at the sensor. Based on this idea, the cost functional (4.3) is formulated as linear superposition of three different components, i.e., the mean and fluctuating components of the adjoint scalar field, and the penalty of the sensor speed. This naturally yields the extra-adjoint equation based on which the sensor trajectory is iteratively optimized. It is confirmed that the cost functional is monotonically decreased in all cases with increasing number of forward-adjoint iterations, and the sensor trajectories eventually converges to the optimal ones.

The resultant optimal trajectories were implemented to a moving sensor and their performances of scalar source estimation were quantitatively evaluated. It was found that the estimation performance of the single sensor moving along the optimal trajectory is drastically improved from that of a stationary sensor, and almost similar to that of 17 stationary sensors. Systematic optimizations with the different weighting coefficients in the cost functional imply that the ratio ϵ between the fluctuation and the mean of the sensitivity, i.e., the adjoint scalar field at the source location, is a primary factor in deciding the estimation performance. Therefore, we also introduced the new cost functional (5.1) which includes ϵ only. It was found that the optimal sensor trajectory under the new cost functional yields essentially the same performance as that under the original cost functional with the best combination of the weighting coefficients for the three components. The advantage of the second cost functional is that there is no adjusting parameter. It was also shown that the optimal sensor trajectory is effective in a wide range of the pulsating frequencies.

The present results support that maximizing the sensor sensitivity with less fluctuation is a promising strategy for optimizing a sensor trajectory. It could be easily extended to find the optimal arrangement of stationary sensors and also optimization of the trajectories of multiple moving sensors. In the present study, it is assumed that the location of the scalar source is known. The localization of a steady scalar source with stationary sensors based on the adjoint-based approach is discussed in a recent study ?, and it is interesting to consider how these techniques can be further extended for localizing a scalar source with a moving sensor. Finally, the present study assumes that the complete information of the spatio-temporal evolution of the velocity field is available. Since this scenario is unrealistic, it is important to take into account the uncertainty of the velocity field and evaluate its impact on the performance of scalar source estimation. These issues remain to be addressed in future work.

Appendix A. Details on the optimization algorithm

We consider the following cost-functional expression for the construction of the optimal sensor trajectory:

$$J_1 = -\alpha_1 \int_0^T c^*(\mathbf{x}^s, t) dt + \alpha_2 \int_0^T \left(c^*(\mathbf{x}^s, t) - \bar{c}^*(\mathbf{x}^s) \right)^2 dt + \alpha_3 \int_0^T \mathbf{u}^m \cdot \mathbf{u}^m dt, \quad (\text{A } 1)$$

where α_i 's serve as weighted constants, and represent the price of the control. The perturbation of the Hamiltonian function H due to the small change of sensor's trajectory \mathbf{x}^m is written as

$$H' = J'_1 + \left\langle \theta \left\{ \frac{\partial c^{*'}}{\partial t^*} - u_j \frac{\partial c^{*'}}{\partial x_j} - \frac{1}{Pe} \frac{\partial^2 c^{*'}}{\partial x_j^2} - \frac{\partial \delta(x_j - x_j^m)}{\partial x_j^m} x_j^{m'} \right\} \right\rangle. \quad (\text{A } 2)$$

The part of the above expression related to the perturbations of the cost-functional, denoted as H'_a , can be shown to be given as

$$H'_a = J'_1 = \left\langle c^{*'} \left\{ -\alpha_1 + 2\alpha_2 \left[c^* - \bar{c}^* \right] \right\} \delta(\mathbf{x} - \mathbf{x}_s) \right\rangle + \int_0^T H'_{\mathcal{B},2} dt + \int_0^T H'_{\mathcal{B},2} x_j^{m'} dt, \quad (\text{A } 3)$$

where we introduce the following useful identities

$$H'_{\mathcal{B},2} = \frac{d}{dt} \left[2\alpha_3 x_j^{m'} \frac{dx_j^m}{dt} \right], \quad (\text{A } 4a)$$

$$H'_{\mathcal{B},2} = -2\alpha_3 \frac{d^2 x_j^m}{dt^2}. \quad (\text{A } 4b)$$

The remaining part of eq. (A 2), denoted as H'_b , can be shown to be written as

$$H'_b = H' - H_a = \left\langle c^{*'} \left[-\frac{\partial \theta}{\partial t^*} + \frac{\partial(\theta u_j)}{\partial x_j} - \left\{ \frac{\partial}{\partial x_j} \left(\frac{1}{Pe} \frac{\partial \theta}{\partial x_j} \right) \right\} \right. \right. \\ \left. \left. - \frac{\partial \theta}{\partial x_j} \delta(x_j - x_j^m) x_j^{m'} \right] \right\rangle + \mathcal{B}, \quad (\text{A } 5)$$

where \mathcal{B} is

$$\mathcal{B} = \left\langle \frac{\partial \theta c^{*'}}{\partial t^*} + \frac{\partial}{\partial x_j} \left\{ -\theta c^{*'} u_j + \frac{1}{Pe} c^{*'} \frac{\partial \theta}{\partial x_j} - \frac{1}{Pe} \theta \frac{\partial c^{*'}}{\partial x_j} + \theta \delta(x_j - x_j^m) \right\} \right\rangle. \quad (\text{A } 6)$$

Substituting eqs. (A 3), (A 5) and the transformation $t^* = T - t$ back into (A 2) yields the following expression

$$H' = \left\langle c^{*'} \left[\frac{\partial \theta}{\partial t} + \frac{\partial(\theta u_j)}{\partial x_j} - \left\{ \frac{\partial}{\partial x_j} \left(\frac{1}{Pe} \frac{\partial \theta}{\partial x_j} \right) \right\} + \left\{ -\alpha_1 + 2\alpha_2 \left[c^* - \bar{c}^* \right] \right\} \delta(\mathbf{x} - \mathbf{x}^s) \right] \right\rangle \\ - \left\langle \frac{\partial \theta}{\partial x_j} \delta(x_j - x_j^m) x_j^{m'} \right\rangle - 2\alpha_3 \int \frac{d^2 x_j^m}{dt^2} x_j^{m'} dt + \mathcal{B}^*, \quad (\text{A } 7)$$

where the boundary term \mathcal{B}^* is given by

$$\mathcal{B}^* = \mathcal{B} + 2\alpha_3 \int_0^T \frac{d}{dt} \left[x_j^{m'} \frac{dx_j^m}{dt} \right]. \quad (\text{A } 8)$$

In order to simplify eq. (A 7), we assume that θ satisfies the following equation:

$$\frac{\partial \theta}{\partial t} + \frac{\partial(\theta u_j)}{\partial x_j} = \left\{ \frac{\partial}{\partial x_j} \left(\frac{1}{Pe} \frac{\partial \theta}{\partial x_j} \right) \right\} + \left\{ \alpha_1 - 2\alpha_2 \left[c^* - \bar{c}^* \right] \right\} \delta(\mathbf{x} - \mathbf{x}^s), \quad (\text{A } 9)$$

which describes the spatial and temporal evolution of θ . We further assume that the above equation is accompanied with the following set of boundary conditions:

$$\theta(\mathbf{x}, t = 0) = 0, \quad \frac{\partial \theta}{\partial x_j} n_j = 0, \quad \text{at } \partial\Omega. \quad (\text{A } 10)$$

so that the boundary term B^* becomes zero. Substituting Eqs. A 9, A 10 back into Eq. A 7 yields

$$\begin{aligned} H' &= \left\langle -\frac{\partial \theta}{\partial x_j} \delta(x_j - x_j^m) x_j^{m'} \right\rangle - 2\alpha_3 \int \frac{d^2 x_j^m}{dt^2} x_j^{m'} dt \\ &= \int_0^T - \left[\left(\frac{\partial \theta}{\partial x_j} \right)_{\mathbf{x}^m} + 2\alpha_3 \frac{d^2 x_j^m}{dt^2} \right] x_j^{m'} dt. \end{aligned} \quad (\text{A } 11)$$

Equation (A 11) indicates that H' is always negative if the sensor trajectory is updated based on the following expression:

$$x_j^{m'}(t) \left(\equiv x_j^{m,n+1}(t) - x_j^{m,n}(t) \right) = \alpha^n \left[\left(\frac{\partial \theta}{\partial x_j} \right)_{\mathbf{x}^m} + 2\alpha_3 \frac{d^2 x_j^m}{dt^2} \right]^n, \quad (\text{A } 12)$$

where the superscript of n indicates the current iteration step and α is a positive coefficient determining the amount of the update in each iteration step.

Appendix B. Details on the cost-functional with ϵ

We seek to derive the evolution equation of θ based on the following cost-functional expression:

$$J_2 = \frac{c_{rms}^*(\mathbf{x}^s)}{c^*(\mathbf{x}^s)} = \frac{\left\{ \frac{1}{T} \int_0^T [c^* - \bar{c}^*]^2 \delta(\mathbf{x} - \mathbf{x}^s) dt \right\}^{1/2}}{\frac{1}{T} \int_0^T c^* \delta(\mathbf{x} - \mathbf{x}^s) dt}. \quad (\text{B1})$$

For convenience, we consider the following identities:

$$w = c_{rms}^*(\mathbf{x}^s) = \left\{ \frac{1}{T} \int_0^T [c^* - \bar{c}^*]^2 \delta(\mathbf{x} - \mathbf{x}^s) dt \right\}^{1/2}, \quad (\text{B2})$$

$$g = \overline{c^*(\mathbf{x}^s)} = \frac{1}{T} \int_0^T c^* \delta(\mathbf{x} - \mathbf{x}^s) dt.$$

The perturbations of w and g in respect to the sensor's location \mathbf{x}^m are given by:

$$w' = \frac{\langle c^{*'} [c^* - \bar{c}^*] \delta(\mathbf{x} - \mathbf{x}^s) \rangle}{T c_{rms}^*}, \quad (\text{B3})$$

$$g' = \frac{1}{T} \langle c^{*'} \delta(\mathbf{x} - \mathbf{x}^s) \rangle.$$

The perturbation of the cost-functional given in (B1) can be found by applying the quotient rule:

$$J_2' = \left[\frac{g w' - w g'}{g^2} \right] = \frac{1}{T} \langle c^{*'} \left\{ \frac{[c^* - \bar{c}^*]}{c^* c_{rms}^*} - \frac{c_{rms}^*}{c^{*2}} \right\} \delta(\mathbf{x} - \mathbf{x}^s) \rangle. \quad (\text{B4})$$

Adopting eq. (B4) and following the same procedure as described in Appendix A yields the following evolution equation for θ

$$\frac{\partial \theta}{\partial t} + \frac{\partial(\theta u_j)}{\partial x_j} = \left\{ \frac{\partial}{\partial x_j} \left(\frac{1}{Pe} \frac{\partial \theta}{\partial x_j} \right) \right\} + \left\{ \frac{c_{rms}^*}{c^{*2}} - \frac{[c^* - \bar{c}^*]}{c^* c_{rms}^*} \right\} \delta(\mathbf{x} - \mathbf{x}^s). \quad (\text{B5})$$

The boundary conditions and the iterative expression for \mathbf{x}^m remain the same as before, given by eqs. (A10) and (A12) respectively.

REFERENCES

- BEWLEY, T., MOIN, P. & TEMAM, R. 2001 Dns-based predictive control of turbulence: an optimal benchmark for feedback algorithms. *J. Fluid Mech.* **447**, 179–225.
- CERIZZA, D., SEKIGUCHI, W., TSUKAHARA, T., ZAKI, T. & HASEGAWA, Y. 2016 Reconstruction of scalar source intensity based on sensor signal in turbulent channel flow. *Flow. Turbul. Combust.* **97**, 1211–1233.
- DAESCU, D. 2008 On the sensitivity equations of four-dimensional variational (4d-var) data assimilation. *Mon. Weather Rev.* **136**(8), 3050–3065.
- HARVEY, D., LU, T. & KELLER, M. 2008 Comparing insect-inspired chemical plume tracking algorithms using a mobile robot. *IEEE. T. Robot.* **24**(2), 307–317.
- HASEGAWA, Y. & KASAGI, N. 2011 Dissimilar control of momentum and heat transfer in a fully developed turbulent channel flow. *J. Fluid Mech.* **683**, 57–93.
- ISHIDA, H., WADA, Y. & MATSUKURA, H. 2012 Chemical sensing in robotic applications: A review. *IEEE Sens. J.* **12**, 3163–3173.
- KEATS, A., YEE, E. & LIEN, F-S. 2007 Bayesian inference for source determination with applications to a complex urban environment. *Atmos. Environ.* **41**(3), 465–479.
- KENNEDY, S. & MARSH, D. 1974 Pheromone-regulated anemotaxis in flying moths. *Science* **184**.4140 **184**, 999–1001.
- KING, S., KANG, W. & XU, L. 2014 Observability for optimal sensor locations in data assimilation. *Int. J. Dynam. Control* **3**(4), 416–424.
- KOWADLO, G. & RUSSELL, R. 2008 Robot odor localization: A taxonomy and survey. *Int. J. Robot. Res.* **27**(8), 869–894.
- MISAKA, T. & OBAYASHI, S. 2014 Sensitivity analysis of unsteady flow fields and impact of measurement strategy. *Math. Probl. Eng.* pp. 1–12.
- MULLER, M. & WEHNER, R. 1994 The hidden spiral: systematic search and path integration in desert ants, *cataglyphis fortis*. *J. Comp. Physiol. A* **175**, 525–530.
- PATAN, M. & PATAN, K. 2005 Optimal observation strategies for model-based fault detection in distributed systems. *Int. J. Control* **78**:18, 1497–1510.
- PUDYKIEWICZ, J. 1998 Application of adjoint tracer transport equations for evaluating source parameters. *Atmos. Environ.* **32**, 3039–3050.
- SOHN, M., REYNOLDS, P., SINGH, N. & GADGIL, A. 2002 Rapidly locating and characterizing pollutant releases in buildings. *J. Air Waste Manage.* **52**, 1422–1432.
- SUZUKI, T. & HASEGAWA, Y. 2017 Estimation of turbulent channel flow at $re_\tau = 100$ based on the wall measurement using a simple sequential approach. *J. Fluid Mech.* **830**, 760–796.
- TRICAUD, C. & CHEN, Y. 2010 Optimal trajectories of mobile remote sensors for parameter estimation in distributed cyber-physical systems. pp. 3211–3215. American Control Conference, Baltimore, USA.
- UCINSKI, D. 2000 Optimal sensor location for parameter estimation of distributed processes. *Int. J. Control* **73**:13, 1235–1248.
- UCINSKI, D. & BARANOWSKI, P. 2013 A parallel algorithm for optimum monitoring network design in parameter estimation of distributed systems. In *Proceedings of the European Control Conference (ECC), Zurich, Switzerland, July 17-19*.
- UCINSKI, D. & CHEN, Y. 2006 Sensor motion planning in distributed parameter systems using turing’s measure of conditioning. In *Proceedings of the 45th IEEE Conference on Decision & Control, San Diego, USA, December 13-15*.
- VERGASSOLA, M., VILLERMAUX, E. & SHRAIMAN, B.I. 2007 "infotaxis" as a strategy for searching without gradients. *Nature* **445**(7126), 406–409.
- VOGES, N., CHAFFIOL, A., LUCAS, P. & MARTINEZ, D. 2014 Reactive searching and infotaxis in odor source localization. *PLoS Comput. Biol.* **10**(10), e1003861.
- WANG, Q., HASEGAWA, Y. & ZAKI, T. A. 2019 Spatial reconstruction of steady scalar sources from remote measurements in turbulent flow. *J. Fluid Mech.* **870**, 316–352.